Cellulose (2021) 28:11625–11643
https://doi.org/10.1007/s10570-021-04252-4

ORIGINAL RESEARCH

Effect of a synthesized chitosan flame retardant on the flammability, thermal properties, and mechanical properties of vinyl ester/bamboo nonwoven fiber composites

M. N. Prabhakar · K. Venakat Chalapathi · Shah Atta Ur Rehman · Jung-il Song

Received: 17 July 2021 / Accepted: 30 September 2021 / Published online: 18 October 2021

Abstract In this study, a chitosan-based bioflame retardant additive (referred to as NCS) was prepared by chemically altering CS with silicon dioxide (SiO_2) via an ion interchange reaction. The effect of NCS on the thermal stability and mechanical properties of vinyl ester/bamboo fiber (VE/BF) composites was studied. The composites were manufactured by a vacuum-assisted resin transfer molding (VARTM) process. Fourier transform infrared (FTIR) spectroscopy, scanning electron microscopy and X-ray diffraction analysis were used to characterize the NCS. The spectral results revealed a new peak at 1560 cm^{-1} corresponding to $NH_3^+-^-O$ Si, indicative of bond between CS and SiO_2. The SEM, and XRD results showed a diverse morphology (coarse surfaces) and a significant decrease in the intensity of the diffraction patterns, respectively, which further supported the formation of NCS. The heat release rate (HRR) of NCS was observed to decrease significantly by 76%, and the residual char content increased by 47% compared with CS. The flame retardant and thermal behavior of the NCS-VE/BF composites were examined by UL-94 standards, microcalorimetry, and cone calorimetry and thermogravimetric analysis (TGA). The results showed a 32% delay in burning time, a 14% enhancement in the limiting oxygen index (LOI), and an 18% decrease in the peak heat release rate (pHRR) and total heat release rate (THR) after incorporation of NCS in the VE/BF composites. The addition of NCS into the VE/BF composites also resulted in improved the mechanical properties of the composites, including the tensile, flexural and impact properties. Overall, the synthesized NCS proved to be suitable for the fabrication of sustainable flame-retardant natural fiber (NF) composites suitable for substructural parts in engineering applications without deterioration of mechanical properties.

Supplementary Information The online version contains supplementary material available at https://doi.org/10.1007/s10570-021-04252-4.

M. N. Prabhakar
Research Institute of Mechatronics, Department of Mechanical Engineering, Changwon National University, 20 Changwondaehak-ro, Uichang-gu, Changwon, Gyeongsangnam-do 51140, Republic of Korea

K. Venakat Chalapathi
Smart Manufacturing Convergence, Changwon National University, 20 Changwondaehak-ro, Uichang-gu, Changwon, Gyeongsangnam-do 51140, Republic of Korea

S. Atta Ur Rehman
Department of Mechanical Engineering, HITEC University, Taxila, Pakistan

J. Song (✉)
Department of Mechanical Engineering, Changwon National Univesity, 20 Changwondaehak-ro, Uichang-gu, Changwon, Gyeongsangnam-do 51140, Republic of Korea
e-mail: jisong@changwon.ac.kr

Keywords Chitosan · Vinyl ester · Bamboo fibers · Thermal stability · Flame retardant

Introduction

Natural fibers (NFs), similar to a composite, with cellulose as the microfibers and hemicellulose and lignin as the matrix, present unique structural properties and play a vital role as reinforcements in composites for engineering applications (Kuranchie et al. 2021). The automobile and aerospace industries have already started using NF composites for structural and substructural parts because of their low density, good mechanical strength, vibration absorption, and ultraviolet ray blocking (Satheesh 2020; Lau et al. 2018). Advances in NFs toward automobile applications have been introduced in the driver and front passenger doors and the rear wing of the new 718 Cayman GT4 Clubsport production vehicles developed by Porsche (bioconcept cars). These materials are formed of an NF composite for economic and energy reasons (Porsche Newsroom 2019).

Although NFs have sufficient mechanical properties and are competitive with synthetic fibers, such as carbon and glass fibers, they have a poor response when used for reinforcement against flammability in polymer composites (Elsabbagh et al. 2018). The incorporation of flame retardant (FR) additives is the most common approach for improving the flame retardancy of NF composites. The effect of various types of FR additives, including ammonium polyphosphate, magnesium hydroxide, zinc borate, and silicon dioxide (SiO_2), on the fire retardancy of NF-based composites has previously been studied (Shukor et al. 2014; Sain et al. 2004; Yingji et al. 2020). However, their inclusion predominantly interferes with the mechanical properties because of their lack of interfacial bonding and compatibility with both the matrix and reinforcement, thereby creating stress concentration points. Hence, improving the fire resistance while maintaining the mechanical strength of NF composites is a challenging task for researchers and industries.

Recently, a few research studies have focused on modifying the chemical interaction of FRs with either NF reinforcement or a matrix to enhance the flame resistance of NF composites without significantly affecting their mechanical properties (Khalili et al. 2017; Kim et al. 2020; Jeencham et al. 2014). Research is still required in this area due to the demand of the present market and the necessity to achieve the desired properties effectively. Bio-FRs, consisting of biomass that provides dense char during combustion, can satisfy this demand. They have attracted attention due to their renewability and the environmentally friendly characteristics, in contrast to the hazardous nature of the existing FRs (Costes et al. 2017). Bio-FRs however do not show high efficiency for polymers and need to be functionalized effectively by chemical modification. Moreover, the selection of a suitable biobased material for flame retardancy and chemical modification is critical. A few biomaterials are available as waste that can enhance flame retardancy, e.g., chitosan (CS), lignin, bone powder, oyster shell powder, and eggshell powder.

CS is an exciting and abundant biowaste polymer that can be chemically modified by graft copolymerization and compounding due to the chemical structure of an amino polysaccharide. The multiple hydroxyl and amidogen groups present in CS promote the flame retardancy behavior of this material. In addition, CS has been used as a char-forming agent in intumescent systems. Recently, Prabhakar et al. used CS in a thermoplastic starch/flax fabric (TPS/FF) system and effectively improved its thermal and flame retardancy properties to reach those of commercial FRs and achieved satisfactory improvements in its mechanical properties (Prabhakar and Song 2018). Additionally, the same authors showed in another study that a novel FR compound produced by effective modification of CS with ammonium polyphosphate significantly enhanced the flame retardant properties of NF composites (Prabhakar et al. 2019; Prabhakar and Song 2020; Shao et al. 2021). Different FRs can be used for the modification of CS, as established in the literature (Li et al. 2020).

Silicon dioxide is an inorganic material with interesting properties such as low toxicity, good biocompatibility, high versatility, high surface area, uniform porosity, and remarkable chemical and thermal stability (Wang et al. 2020; Huang et al. 2019). In addition, silicon dioxide can act as an effective FR for polymer composites, by phase condensation and formation of an inorganic char. In wood fiber polymer composites, silicon dioxide decreases the heat release rate (HRR) and total heat release rate (THR) (Pan et al. 2014). Therefore, this material has attracted attention

for use in commercial applications in the civil engineering, construction, building, electrical, transportation, aerospace, defense, textile, and cosmetic industries (Hamdani et al. 2009). Moreover, silicon dioxide alone may be able to play a dual role in enhancing the mechanical and flame retardancy properties of NF composites.

Considering the above, this study focused on the preparation of a novel FR additive (referred to as NCS) by a simple chemical approach using CS and silicon dioxide. The combination of CS and silicon dioxide has been studied in other research areas, such as the removal of GO. However, no information is available on the synthesis of a CS-based silicon dioxide FR additive (NCS). This study further investigated the effect of NCS on NF-based polymer composites (vinyl ester/bamboo fiber (VE/BF)). The chemical features of the synthesized NCS compounds were characterized via scanning electron microscopy (SEM), Fourier transform infrared (FTIR) spectroscopy, X-ray diffraction (XRD), thermogravimetric analysis (TGA), and microcalorimetry. The flammability, thermal properties, and mechanical properties of the NCS additive-incorporated VE/BF composites were examined via a horizontal burn test (HBT), cone calorimetry, TGA, XRD, FTIR, and universal testing machine (UTM) analysis. The results showed enhancements in the fire retardancy and thermal stability of the VE/BF composites as a result of NCS incorporation. Simultaneously, the tensile, flexural and impact properties of the VE/BF composites were also observed to increase slightly in the presence of NCS, which was the main objective of this study.

Materials and methods

Materials

The following materials were used in this study without any modifications: VE (viscosity 150 cps and specific gravity 1.03), methyl ethyl ketone peroxide (MEKP), cobalt naphthalate (CN), Teflon sheets (CCP composites, Korea); bamboo nonwoven fabric (strength: 45.1 MPa, reinforced size: 200 × 200 × 0.39 mm (Sungchang Industries, Korea)). CS (molecular weight ≈ 600,000, viscosity: 50–800 mPa, degree of deacetylation 80–95% (Kwang Jin Chemical Co. Ltd., South Korea); and silicon dioxide (extra pure) (Samchun Chemical Co., Korea).

Preparation of NCS

First, the required amount of CS flakes (10 w/v) were dispersed in 2% acetic acid solution with ultrapure water and stirred at 500 rpm for 4 h at 60 °C to obtain a homogeneous CS solution. Subsequently, a silicon dioxide solution (2.5 w/v) was added to the CS solution (equivalent to the molar ratios of SiO_2 in accordance with CS), and stirring was continued at 500 rpm and 80 °C for an hour. The end of the reaction was determined by the formation of a yellowish-brown thick precipitate, which was then cooled to room temperature and subjected to vacuum filtration. The obtained product was thoroughly washed with deionized water and dried overnight (≈ 6 h) in an oven at 70 °C. Finally, the dried flakes were finely ground into a powder using a ball mill.

Manufacturing NCS–VE/BF composites

The vacuum assisted resin transfer molding (VARTM) process was used to manufacture the NCS–VE/BF composites, as discussed by Chalapathi et al. (2020). The NCS was stirred mixed with the VE resin by using planetary centrifugal mixer (Thinky mixture (model: ARM-310, Japan) at 2000 rpm for 10 min. Six layers of bamboo nonwoven fabrics were stacked on a Teflon surface inside a vacuum bag; the resin was allowed to flow through the fabric with the help of 0.4-MPa vacuum pressure in the VARTM process. The infused wet composites were subjected to a precuring process at room temperature for 5 h, followed by postcuring at 60 °C for 3 h in a composite curing oven (Fleta 5, LK LAB Co., Ltd, Republic of Korea). The overall preparation of NCS and the manufacturing process of the NCS–VE/BF composites are depicted in the schematic illustration, as depicted in Scheme 1.

Testing and characterization

NCS characterization

The details of the characterization instruments adopted for analyzing the fabricated NCS compound are as follows: a scanning electron microscope with an ion sputter coater (Model: Emcrafts cube 2,

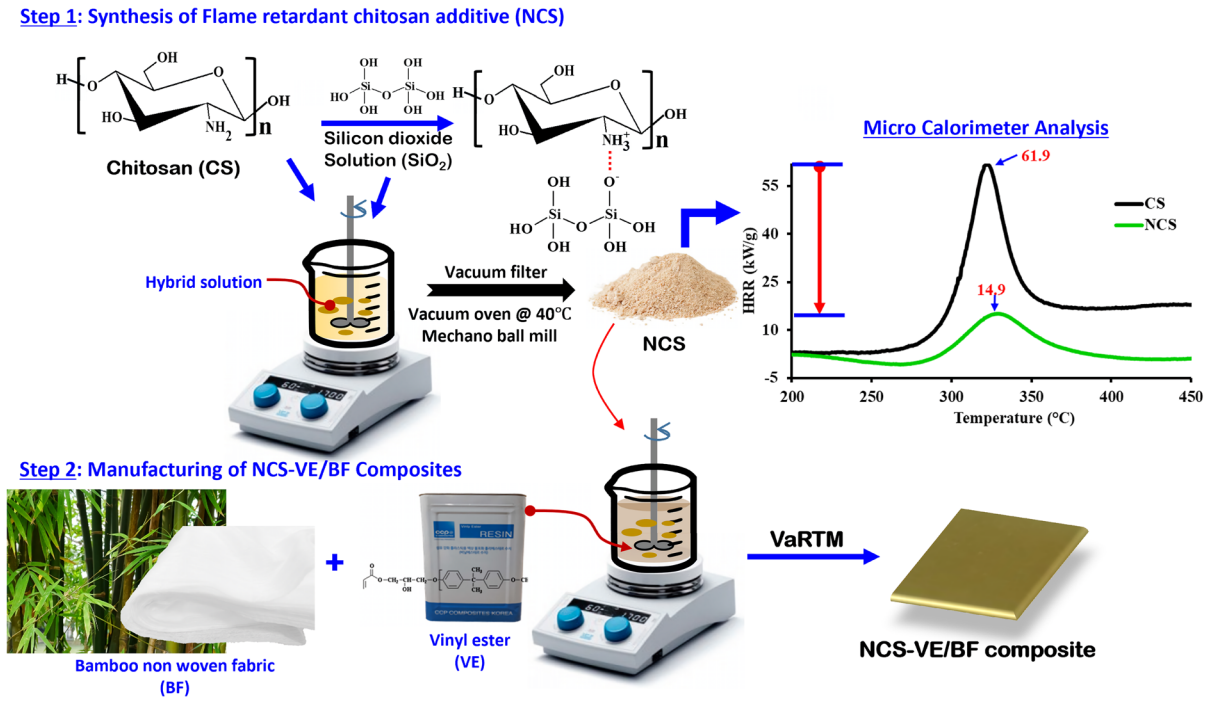

Scheme 1 Chemical reaction process for synthesis of NCS and scheme of manufacturing of NCS–VE/BF composites

EMCRAFTS Co., Korea) was used for microanalysis. A particle size analyzer (Model: Malvern Mastersizer) was used for particle size analysis. An FTIR spectrometer (FT-IR-6300, United Kingdom) using the KBr disk method was employed for spectral analysis. An X-ray diffractometer (Model: Bruker, D8 Discover) with Ni-filtered Cu Kα radiation at a speed of 5°/min, a current of 30 mA, and a range of 0°–50° was used for XRD analysis. A particle size analyzer (Model: Mastersizer 2000, Malvern Panalytical Ltd., United Kingdom) was used to calculate the mean particle size and the particle size distribution. An elemental analyzer (Variable EL, Analyzensysteme GmbH Co., Ltd., Germany) was employed to detect the elements. A thermogravimetric analyzer (Model: TGA Q600, TA instruments) was used at a heating rate of 20 °C/min under an inert atmosphere with a temperature range of 30–700 °C for thermal analysis. A microcalorimetry test apparatus (Model: Microcalorimeter (Federal Aviation Administration, Fire Testing Technology (FTT), United Kingdom)) was utilized to calculate the HRR and THR rates as per ASTM D 7309 standards.

NCS–VE/BF composites characterization

The details of the testing instruments used to analyze the fabricated NCS–VE/BF composites are as follows: a UTM (Model: R&R, Inc., Korea) was used to conduct tensile (250 × 25 × 3 mm) and flexural (support span: 64 mm (16 times the thickness)) tests according to ASTM D638 and ASTM D790-03 standards, respectively. An Izod impact instrument (QC-639F, Cometech Testing Machine Co., Ltd., China) with an 11-J impact hammer was used to conduct impact tests according to ASTM D256. Horizontal and vertical burn tests were performed to examine the flammability properties of the samples by calculating the burn time, rate, and level relative to the UL94 standard. The limited oxygen index (LOI) percentage of the composites was measured using an oxygen index instrument (FESTEC International Co. Ltd., Korea) as per ASTM D2863-97 standards (sample size: 100 × 6.5 × 3 mm^3) at room temperature. A cone calorimeter (Fire Testing Technology, United Kingdom) was employed according to the ASTM E1354/ISO 5660 standard (100 × 100 × 3 mm) at 50 kW/m^2 to determine the

external heat flux for examining the flammability and smoke properties.

Results and discussion

Experimental results for NCS

Spectral analysis

The spectral peaks of NCS and the related raw materials, CS and silicon dioxide additives, are shown in Fig. 1. In the CS spectrum, the spectral peaks appear at 3500–3300, 1620, 1430,1378, 1160, 1079, and 1032 cm^{-1}, corresponding to –OH and $–NH_2$, C=O, O–H, C–N(amide), C–O (bridge oxygen), (C–O–C assym), and (C–O–C sym) (Lustriane et al. 2018). In addition, in the silicon dioxide spectrum, the peaks observed at 1051 and 781 and 1600–1700 cm^{-1} correspond to the bending vibrations of Si–O and –OH, respectively. In contrast, the spectrum of the synthesized NCS compound exhibits peaks corresponding to both the raw compounds, with peaks attributed to CS at 3427 and 1079, and peaks attributed to silicon dioxide at 776, and 683 cm^{-1}. Most importantly, several changes occurred in the NCS spectrum as briefly described below: new peaks appeared at 1628 and 1560 cm^{-1}, suggesting the formation of a chemical bond between NH_3^+ and silicon dioxide Si- (Hassan et al. 2019; Budnyak et al. 2014); the spectral peaks of silicon dioxide and CS at 891 cm^{-1} and the CS peak at 762 cm^{-1} disappeared (Yeh et al. 2007); the broad CS peaks at 2918 and 2873 cm^{-1} sharpened and were observed at 2917 and 2849 cm^{-1} and the CS peak at 1382 cm^{-1} shifted to 1406 cm^{-1}. Notably, the intense peak at 1079 cm^{-1} may be associated with Si–O–Si and Si–O–C, suggesting interaction and bond formation. Overall, the FTIR spectrum suggested the occurrence of ion exchange between CS and silicon dioxide to form the NCS compound, which is verified by the XRD and SEM analysis discussed in the following sections.

XRD analysis

The XRD patterns of NCS and the corresponding raw materials (CS and silicon dioxide) are shown in Fig. 2a. The pattern of silicon dioxide exhibits well-defined sharp diffraction peaks at 20.8°, 26.6°, 36.5°, 42.4°, 45.5°, and 49.9°, clearly indicating a crystalline structure (Kumar and Koh 2012). That of CS presented typical semicrystalline peaks at approximately 10° and

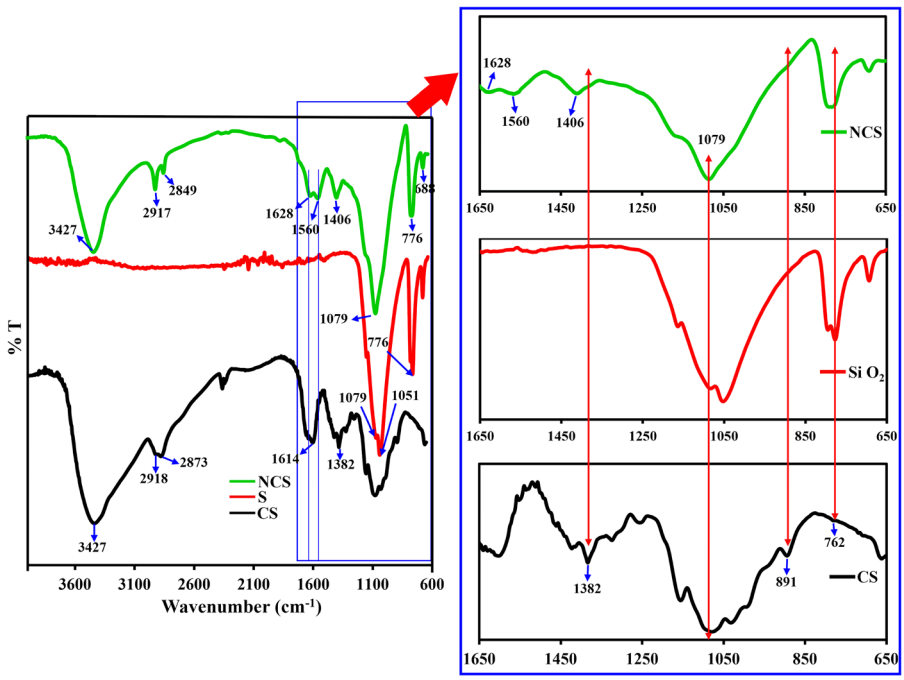

Fig. 1 Spectral analysis results of CS, SiO_2 and NCS compounds

20° (Zang, Yan, Shen, Fang, Zhang, & Wang). In the spectrum of the NCS compound, the diffraction peaks were completely different from those of CS, with sharp crystalline peaks at 20.8°, 26.6°, 36.5°, 39.4°, 40.2°, 42.4°, and 45.8°, resembling the silicon dioxide diffraction pattern. However, the intensities of the two main peaks of silicon dioxide at 20.8° and 26.6° were 20,978 and 106,065 respectively, and drastically decreased to 16,345 and 66,383 for the NCS compound. Furthermore, the calculated crystalline diameter using Scherrer equation $D = K\lambda/\beta \cos\theta$ (where D = crystallites size (nm), K = 0.9 (Scherrer constant), λ = 0.15406 nm (wavelength of the x-ray source), β = FWHM (radians), θ = peak position (radians) as shown in Fig. 2a, was 47 nm for NCS, 2.27 nm for CS and 55.75 nm for SiO_2. Therefore, the overall changes in the NCS diffraction patterns confirm the chemical reaction between CS and SiO_2 to form the NCS compound and verify the spectral analysis.

Microanalysis

Microscopic images of NCS and the corresponding raw materials (CS and silicon dioxide additives) are shown in Fig. 2b. Silicon dioxide particles possessed a smooth metallic surface morphology without any voids. The particles varied in size; two major particle sizes were observed in the micrograph, i.e., ∼ 2–10 m and ∼ 10–20 m. CS exhibited a rough and continuous morphology without voids, and the particle size ranged from 25–35 m. However, the micrograph of NCS showed an entirely different morphology than those of CS and the SiO_2 compound, confirming the formation of a new compound upon reaction between them. The NCS powder particles showed a coarse surface with continuous morphology without any

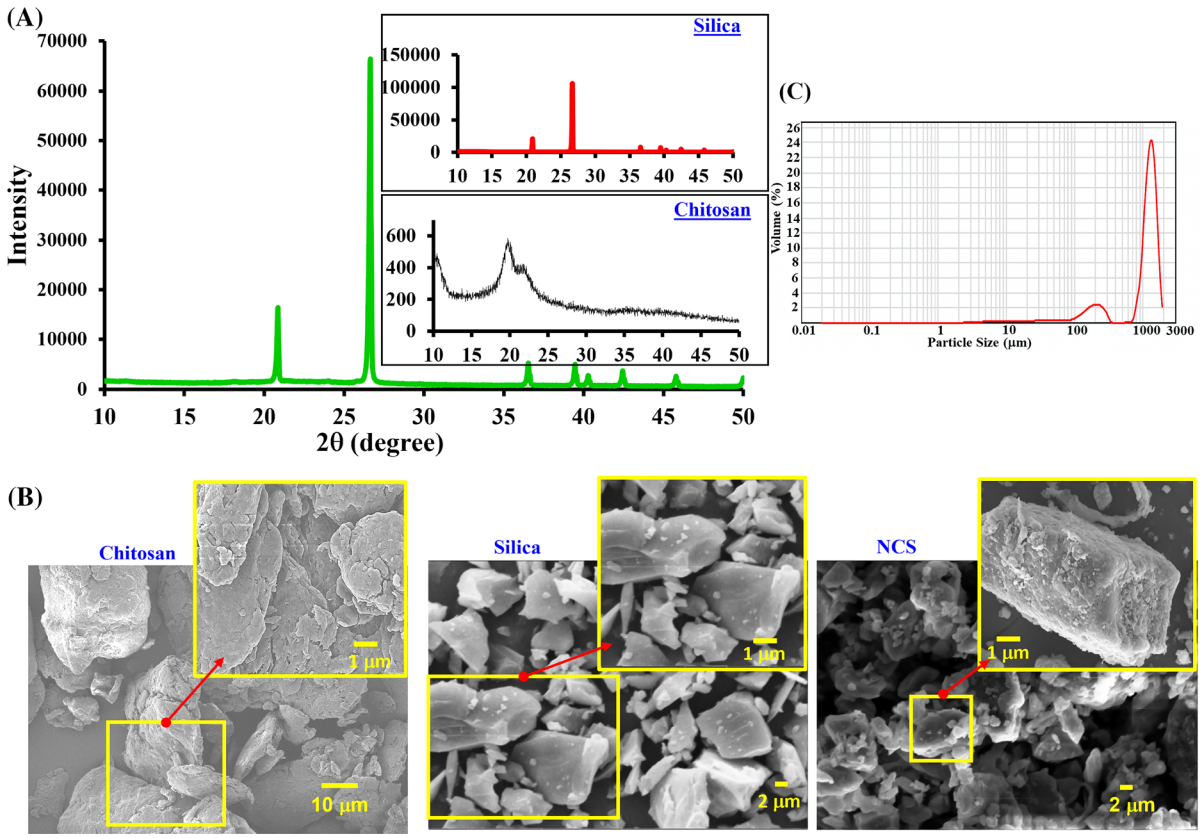

Fig. 2 **a** Powder XRD analysis of CS (D = 2.27 nm, 19.5°, 572 counts), SiO_2 (D = 55.75 nm, 20.8° = 20,620 counts, 26.6° = 106,065 counts) and NCS (D = 47.02 nm, 20.8° = 16,345 counts, 26.6° = 66,383 counts) compounds, **b** SEM micrographs of CS, S and NCS compounds, and **c** particle size analysis of the NCS compounds

voids. However, the shape of the particles seemed slightly in between those of the CS and SiO_2 compounds. In addition, it was observed that 2–5 m particles adhered to the surfaces of larger particles and formed lumps, making the surface appear rougher. In fact, dual-sized NCS particles of approximately 1000 and 200 m could be seen in the micrographs similar to silicon dioxide particles. Overall, the morphology of the synthesized NCS particles showed a unique morphology and was clearly different from those of reactants CS and SiO_2. Hence, the morphology findings provide further details and support the spectral and XRD analysis.

Particle size analysis

The particle size distribution of the NCS additive is shown in Fig. 2c. Consistent with the morphology analysis, the particle size analysis also exhibited the dual average particle sizes of NCS particles of approximately 200 and 1200 μm, with volume percentages of 2 and 24, respectively. The NCS particle size was controlled by the mechano ball mill technique using a ball-to-weight ratio of 1:5 and the process was implemented out for 48 h at 60 °C (with all moisture removed). Interestingly, the mechano ball mill process produced precise NCS particles with sizes of approximately 1258 μm and 208 m at volume percentages of 22 and, 2 respectively.

Elemental analysis

The elemental compositions of CS and the NCS compound include carbon, hydrogen, nitrogen, and sulfur, as tabulated in Fig. 2d. CS consists primarily of C, H, and N in amounts of 42%, 6.88%, and 8.17%, respectively. However, a significantly reduced concentration of the same elements was found in the synthesized NCS, which included C (22.33%), H (5.12%), and N (3.38%). In addition, 0.46% of silicon was also observed in NCS which represents a silicon moiety obtained by the chemical reaction with SiO_2. Hence, the elemental analysis further supports the spectral and diffraction analysis regarding the formation of NCS compounds.

Thermal analysis

The thermograms of the CS and NCS additives are shown in Fig. 3a. CS exhibited a two-step thermal degradation behavior; the initial step at < 100 °C was due to the exclusion of the absorbed water. The prominent pyrolytic degradation of the CS molecule started at 350 °C and continued to 700 °C and was attributed to the dehydration of saccharide rings and decomposition of the acetylated and deacetylated units. The multiple hydroxyl groups present in CS are responsible for forming a dense char of almost 30% in the form of a residue at 700 °C. However, the NCS compound showed a different trend the CS, with the total thermal degradation process occurring in a single-step. In the initial stages the NCS compound maintained a constant weight without degradation, and the decomposition temperature was above 100 °C. Further degradation proceeded with a marginal decrease in weight loss. This slight thermal degradation could explain the lower amount of volatile products, including moisture, present in the NCS compound. However, the majority of degradation occurred above 300 °C, with a weight loss of approximately 20% resulting from decomposition of the main constituents, such as CS moieties and aqueous silicon dioxide, along with their bonds, but in the case of CS, the weight loss was almost 60%. The drastic variation between CS and NCS clearly indicates to the significant slowdown of the thermal degradation process due to the synergistic effect of silicon and CS in NCS. It may be understood that during the thermal degradation process, the silicon moiety present in the NCS protects the material from thermal degradation. In addition, NCS produced nearly 56% char residue at 700 °C, showing substantial thermal stability. The CS and SiO_2 moieties present in NCS probably produce a combination of carbonaceous and SiO_2-based char residues thereby forming dense char.

Figure $3a_1$ presents the oxidative thermal degradation of the NCS compound. As can be observed from the figure, the thermal oxidation of NCS occurred in three steps in the temperature range of 30–400 °C. A gradual decline was observed from the initial point of the thermograms and continued to 240 °C. Almost 20% of weight loss occurred at initial degradation temperatures > 240 °C without a drastic decline, which explains the slow evaporation of surface moisture, trapped water and volatile compounds.

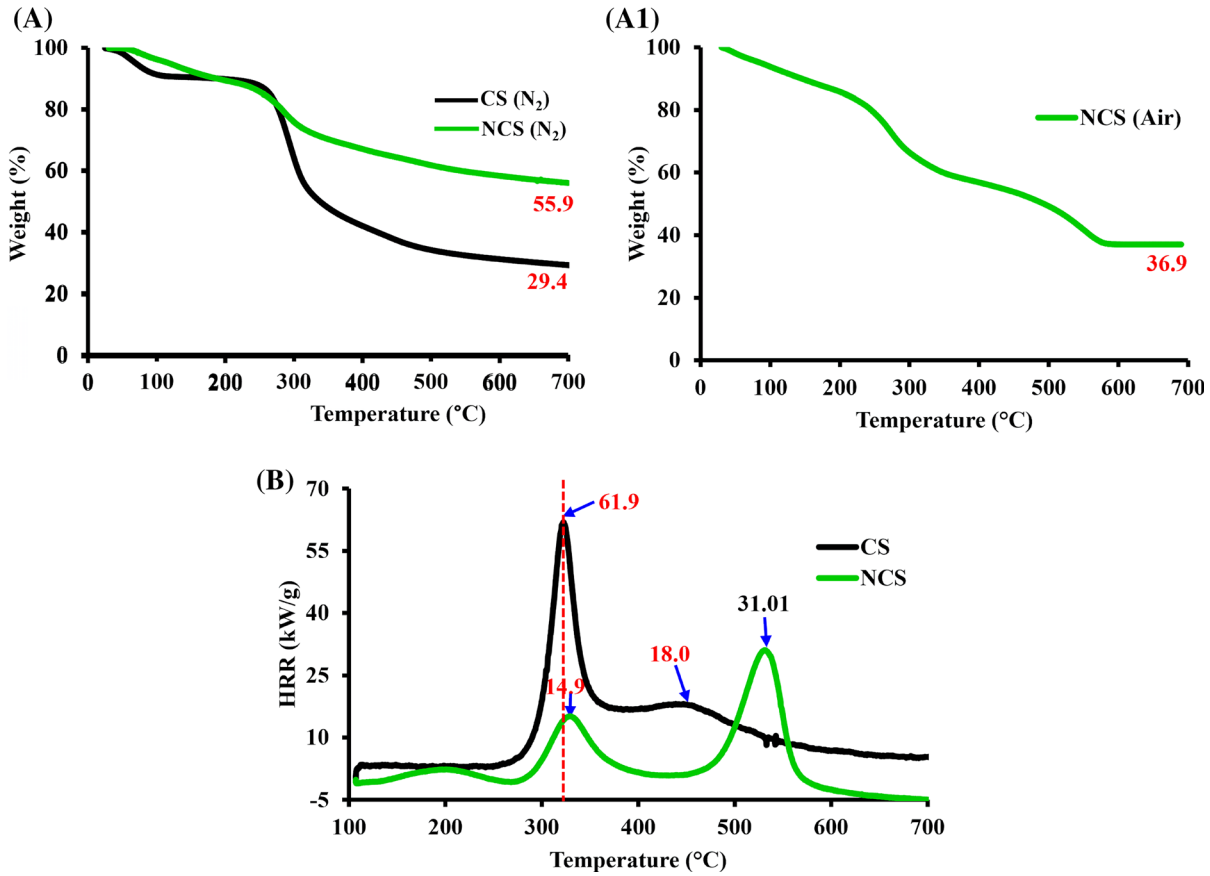

Fig. 3 TG profiles of CS and NCS under N_2 (**a**), TG of NCS under air ($\mathbf{a}_1$), and (**b**) microcalorimeter profiles of the CS and NCS compounds

However, drastic thermal degradation occurred at < 240 °C by the thermal degradation of saccharide rings, which exactly resembled the CS thermal degradation behavior in a nitrogen atmosphere. The deceleration of the thermal degradation process was observed in the range of 300 to 580 °C with almost 15% of weight loss. Interestingly, the thermal degradation process completely stopped at temperatures above 580 °C and there was no further degradation up to 700 °C. The silicon moiety in the NCS compound may be responsible for the increased thermal degradation temperature and char residue of 37%. Over time, the NCS compound showed a significant reduction in the thermal degradation process and formed more char residue in both inert and air atmospheres, consistent with the thermal stability.

HRR analysis

The HRR peaks of the CS and NCS additives are shown in Fig. 3b**,** and it can be observed that both CS and NCS produced two peak HRRs (pHRRs) during the combustion analysis. CS burned rapidly during the microcalorimetry analysis due to its sensitivity under fire exposure, and it displayed the highest pHRR of 61.9 kW/g at 321 °C. The second pHRR of 18 kW/g was generated at 538 °C due to thermal stresses. In addition, the NCS showed a remarkably different flammability behavior than that of CS. The synergistic effect of CS and SiO_2 effectively decreased the pHRR value to 14.9 kW/g, which is a severe decrease of approximately 75% compared to an equal amount of CS (Shao 2014). Moreover, the pHRR of NCS was observed at a delay of 10 °C compared to CS, which further supports the higher fire retardant behavior of the NCS compound. Crack formation due to thermal

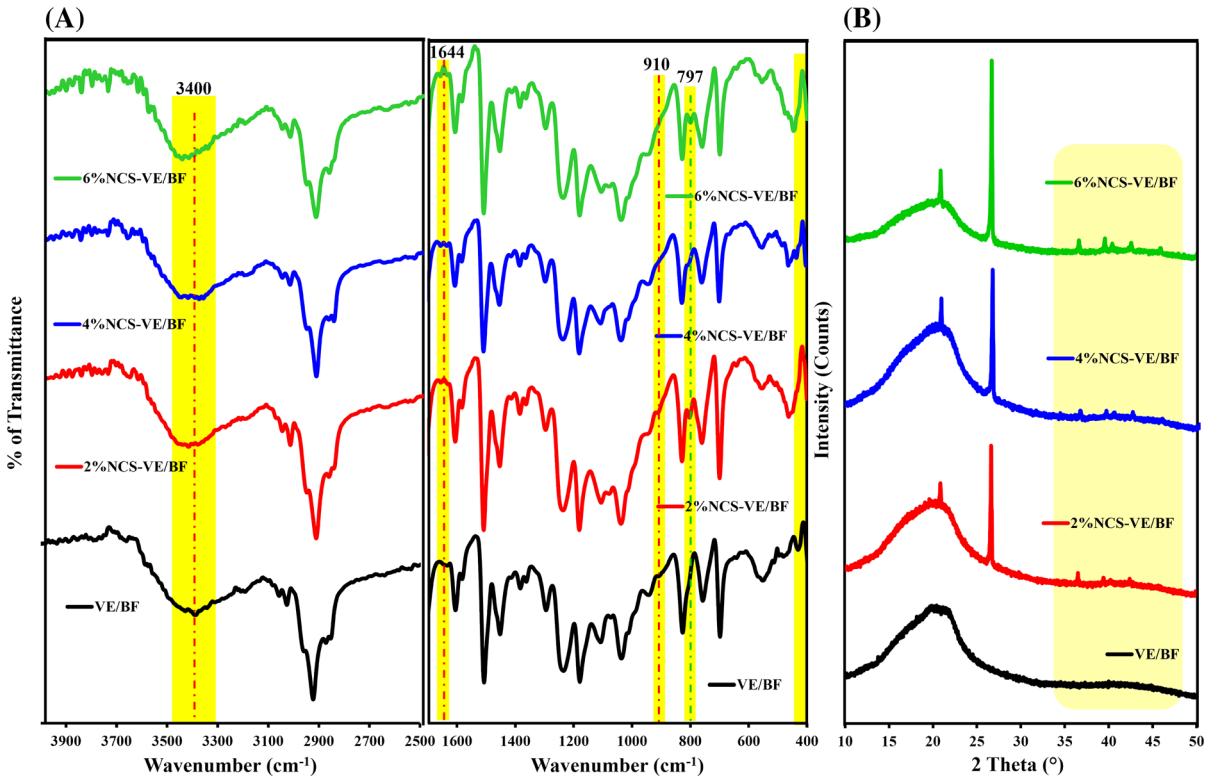

Fig. 4 **a** FTIR spectra of VE/BF and 2–6% NCS loaded VE/BF composites and **b** powder XRD spectra of VE/BF (19.9° = 6215 counts) and 2% (26.6° = 8138 counts), 4% (26.6° = 8825 counts), and 6% (26.6 = 10,262 counts) NCS-loaded VE/BF composites

stress in the dense char was also observed in NCS. However, it occurred almost 90 °C later than that in CS. Overall, a significant improvement in the fire retardant property of the NCS compound was achieved owing to the production of carbonaceous and silicon-based char by the action of silicon dioxide and CS moieties by the synergistic effect of through the condensed phase.

Experimental results for NCS–VE/BF composites

Spectral (FTIR) analysis

Spectral (FTIR) analysis was performed to verify the possible interaction (chemical or physical) between NCS and the constituents of VE/BF composites. The spectral analysis data of VE/BF and various % NCS–VE/BF composites are shown in Fig. 4a and Supplementary section Fig. S1. The VE/BF composite spectrum consists of the combined spectral peaks of VE and BF at 1713, 2920, and 1032 cm^{-1} corresponding to the carboxyl group of ester, methyl groups (C–H), and glucopyranose rings (C–O). Notably, the spectral peak intensity at 1713 cm^{-1} increased, clearly signifying the interaction of BF with VE (Sefadi and Luyt 2012). For the NCS-VE/BF composite, the combination peaks of VE, BF and NCS were clearly observed in the spectrum as shown in Fig. 3b. In fact, several apparent changes occurred in the spectrum of the VE/BF composites after the addition of NCS. For instance, with the disappearance of spectral peaks at 910 and 1644 cm^{-1}, the spectral peak at approximately 3400 cm^{-1} corresponding to the –OH groups, shifted to slightly higher wavenumbers with the percentage increase in NCS and the formation of a new peak at 797 cm^{-1}. Hence, these spectral alternations might be evidence for the interaction of NCS with the constituents of the VE/BF composites.

XRD analysis

The XRD patterns of the VE/BF and NCS–VE/BF composites are shown in Fig. 4b. The pattern of the

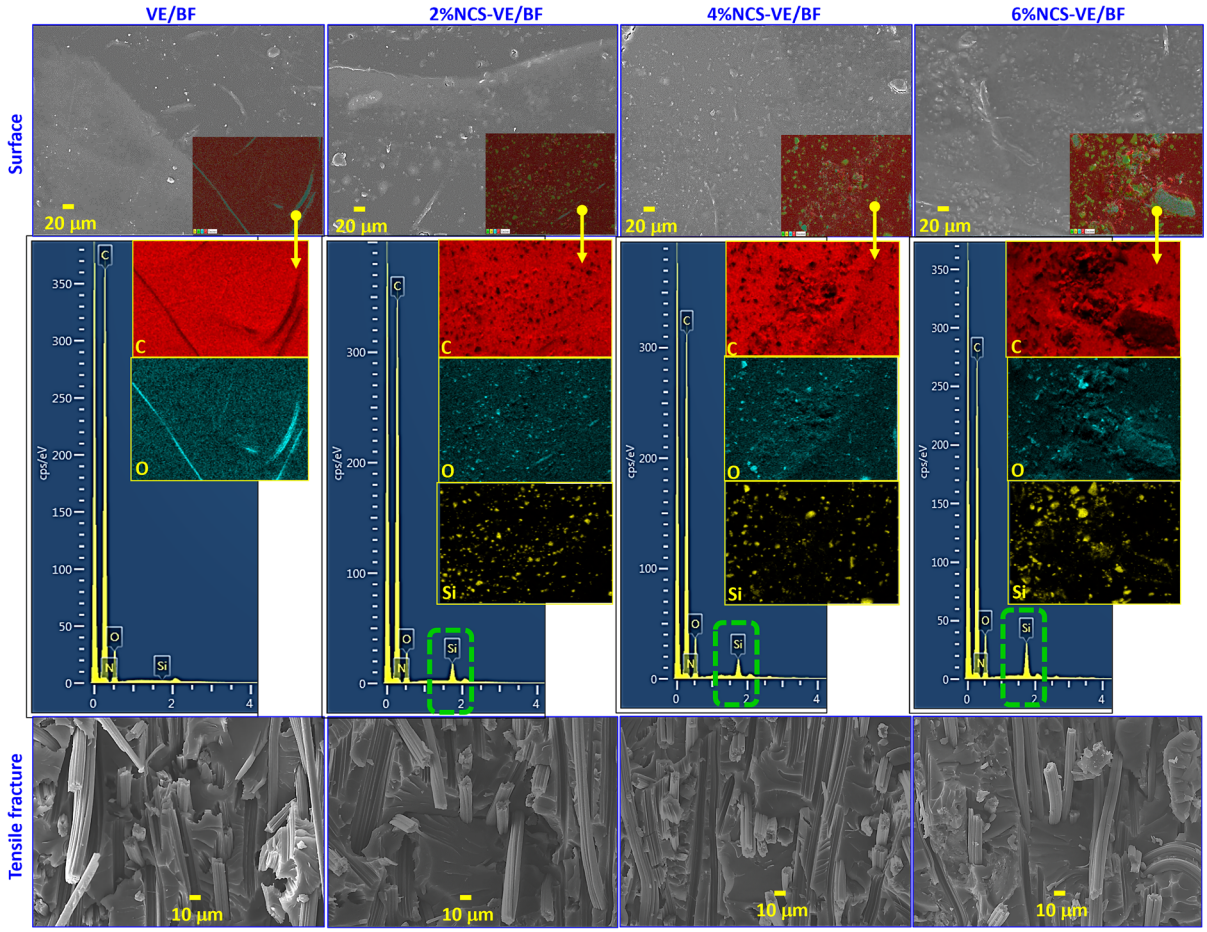

Fig. 5 SEM surface micrographs and EDX analysis of VE/BF and 2–6% NCS-loaded VE/BF composites and tensile fracture surface micrographs of VE/BF and 2–6% NCS-loaded VE/BF composites

VE/BF composite shows a broad peak at approximately 19.9° with an intensity of 6215 counts. This suggests the noncrystallinity of the VE/BF composite with an amorphous structure. However, the addition of the NCS additive significantly influenced the structural behavior of the VE/BF composites. Sharp diffraction peaks appeared at 20.8°, 26.6° (predominant), 36.5°, 39.4°, and 42.4° for the 2 wt.% NCS-loaded VE/BF composite, which gradually become predominant with an increasing percentage of NCS. These sharp peaks indicate the induced effect of the NCS crystalline structure and the intensity of the peaks was clearly observed in the XRD pattern of the 6% NCS-VE/BF composite. The appearance of crystalline peaks of the NCS compound also indicates the homogeneous distribution of particles throughout the VE/BF composite. Overall, the XRD results further support the spectral analysis for the interaction/influence of NCS with VE/BF composites.

Microanalysis

The plain surfaces and tensile fractured surfaces of the VE/BF and NCS–VE/BF composites were examined by microscopic analysis, and the micrographs are shown in Fig. 5. The plain surface SEM images clearly present the differences in the structural morphology of the VE/BF and NCS–VE/BF composites. The surface morphology of the VE/BF composites was almost smooth, with a few impurities on the surface, which may form at the time of cutting the test specimen. In addition, the surface of the NCS-loaded VE/BF composites appeared coarse, and some of NCS particles trapped in the VE resin were observed on the

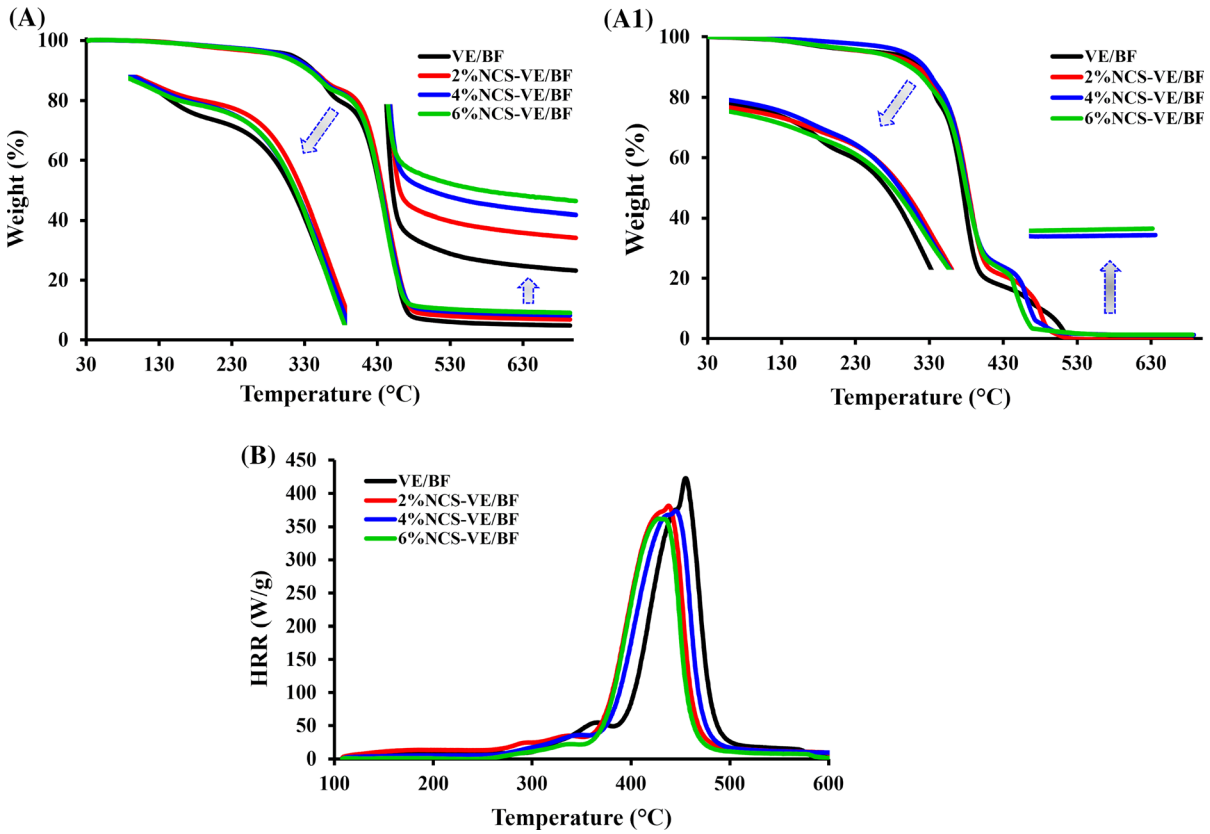

Fig. 6 TG profiles of VE/BF and 2–6% NCS-loaded VE/BF composites under N_2 (**a**), air (**a**$_1$) and microcalorimeter data (**b**). Magnified areas of the maximum temperature zone and the char residue at 700 °C

surface. This rough behavior gradually become predominant, and even the number of particles on the surface increased with increasing wt.% NCS in the composites. Furthermore, the EDX mapping supports the microanalysis by exhibiting the distribution of NCS additive in the composites. It is very clear in the mapping that there are no yellow particles in the VE/BF composites, but in the NCS inclusion, yellow particles appeared and increased the density with increasing percentage. Similarly, in the EDX graphs, it can be observed that VE/BF contained mainly carbon (C) and oxygen (O), whereas the NCS loaded with silicon (Si) appeared and increased with an increasing percentage of NCS by decreasing the carbon content.

Thermal analysis

The TGA curves of the VE/BF and NCS–VE/BF composites under pyrolytic and oxidative atmospheres are shown in Fig. 6 and important data are tabulated in Table 1. In the pyrolytic atmosphere, the trends of all the composite thermograms are similar, with marginal differences in the initial degradation process. An approximately 1% weight loss occurred below 150 °C, corresponding to the degradation of the sample by the evaporation of free water. The zeolite present in the BF is responsible for enhancing thermal stability. Hence, slight degradation was observed at approximately 350–400 °C for the VE/BF composites. In fact, the higher thermal stability of NCS effectively induced an even smaller reduction in the thermal degradation of VE/BF, as shown in the figure. After major degradation, the char residue remaining at 700 °C for the VE/BF and 2, 4, and 6 wt.% NCS–VE/BF composites was 4.7%, 6.8%, 8.2%, and 9.0% respectively. Therefore, the introduction of NCS can decelerate the decomposition of the VE/BF composites by forming approximately 47% char residue compared to the pure VE/BF composite.

Table 1 TG profiles of VE/BF and 2–6% NCS-loaded VE/BF composites

Sample	Thermogravimetric analysis					
	Nitrogen			Air		
	T_{onset} 10% [°C]	T_{max} 75% [°C]	Residue wt.% @ 700 °C	T_{onset} 10% [°C]	T_{max} 75% [°C]	Residue wt.% @ 700 °C
VE/BF	341	454	4.7	317	393	0
2%NCS-VE/BF	341	457	6.8	317	409	0
4%NCS-VE/BF	341	456	8.2	324	421	1.2
6%NCS-VE/BF	336	454	9.0	306	417	1.3

Table 2 HBT, vertical burning test, LOI, microcalorimetry and cone calorimetry results of pure VE/BF and 2–6% NCS-loaded VE/BF composites

Sample	Air				$O_2 + N_2$			
	Horizontal burn test		VB Test		LOI	Calorimeter		
	Burn time [sec]	Burn rate [mm/sec]	Dripping	Rating	(%)	pHRR [W/g]	THR [kj/g]	FIGRA W/g. s^{-1}
VE/BF	1.53	0.66	N	NR	18.9	422.7	25.5	0.92
2%NCS-VE/BF	2.32	0.49	N	HB	26.4	381.5	24.7	0.86
4%NCS-VE/BF	2.35	0.48	N	HB	27.6	373.6	23.3	0.84
6%NCS-VE/BF	2.54	0.43	N	HB	28.3	361.9	20.7	0.83

In an oxidative atmosphere, the trends of the thermograms were almost similar, and no apparent differences were observed between the degradation behavior of VE/BF and NCS–VE/BF composites. However, the major degradation process in the VE/BF composite started earlier (at 350 °C) than that of the NCS–VE/BF composites (at 359 °C). The degradation of the VE/BF composites continued progressively until the end. In addition, the inclusion of NCS showed a small impact on maintaining marginal dominance throughout the degradation process. The VE/BF composites combusted completely without leaving any char residue at 700 °C. However, even under an oxidative atmosphere and a high percentage of NCS loading, the composites were not fully combusted, and an approximately 1.5 wt% stable residue (silicon-based carbonaceous char) remained, indicating the thermal stability of the composites.

Flame retardancy

UL-94 (HB and VB Test) and LOI test The horizontal burning time and rate of the VE/BF and NCS–VE/BF composites are tabulated in Table 2. The weak flame resistance of both VE and BF induced rapid burning of the VE/BF composites with a burn time of 1.53 min. As expected, inclusion of NCS increased the burning time of the VE/BF composites. The addition of 2 wt.% NCS delayed the burn time to 2.32 min, an approximately 34% delay compared to that of the VE/BF composites and this trend gradually increased for 4 and 6 wt.% NCS and delayed the time to 2.35 and 2.54 min, respectively. The formation of char residue especially carbonaceous silicate char could slow fire propagation, thereby protecting the underlying material (Shen et al. 2014). In addition, as discussed in Mechanical performance Section the inclusion of

NCS into the composites effectively improved the modulus representing the stiffness of the composites. In general, stiffer materials could resist heat (Atta ur Rehman et al. 2018), which is one of the factors in the fire triangle. Hence, NCS could also decrease the burning rate by increasing the stiffness of the composites. The flammability ratings of the NCS-VE/BF composites obtained by the vertical burn test and LOI results are tabulated in Table 2. The incorporation of NCS could not make the VE/BF composites reach VB levels; all the composites burned completely. However, as shown in the digital images during the vertical burn test (Fig. S2), the burning time decreased with NCS loading in the VE/BF composites. An LOI test was carried out to further evaluate the flame retardancy of the NCS-VE/BF composites and the results are shown in Table 2. The VE/BF composite showed a low LOI of 18.9. However, NCS loadings significantly increased the oxygen levels to initiate burning. The LOI values of the 2, 4, and 6% NCS-VE/BF composites were showing 28, 31 and 33% respectively, which are much higher the oxygen level in living environments. Overall, NCS could effectively function as an FR for VE/BF composites.

Microcalorimetry and cone calorimetry analysis Microcalorimetry and cone calorimetry analysis was carried out to obtain HRR, THR, FIGRA, CO_2P, COP and SPR data to further understand the flammability behavior of the NCS–VE/BF composites, and the obtained data are shown in Fig. 6b, Table 2 and Fig. S2. Figure 6b shows that, the attained data are in agreement with the HBT and LOI results. The pHRR of the VE/BF composite was as high as 422.7 W/g. The inclusion of NCS (2–6 wt.%) into the VE/BF composite considerably decreased the pHRR to approximately 381.5, 373.6, and 361.9 W/g. NCS consists of multiple hydroxyl groups, SiO_2 and amino group supports to produce carbonaceous silicate char and inert gas thereby flattening the HRR. A similar trend was followed by THR data, showing values of 25.5, 24.7, 23.3, and 20.7 kJ/g for the VE/BF and 2–6% NCS–VE/BF composites and concluding an almost 18% reduction in THR with the addition of NCS. The fire growth rate index (FIGRA) was used to estimate the burning tendency of the materials. The FIGRAs of VE/BF and 2–6% of NCS-VE/BF composites were 0.86, 0.84 and 0.83 W/g.s^{-1}, respectively, as shown in Table 2, which is lower than that of VE/BF (0.92 W/g.s^{-1}), clearly demonstrating that the additon of NCS could enhance the flame retardancy of the VE/BF composite. In addition, the incorporation of NCS into the VE/BF composite could evidently slightly reduce the CO_2P and COP yields by approximately 20%. Similarly, the smoke particulates and flammable gases decreased with NCS. The pSPR of VE/BF was 0.29 m^2/s (Fig. S2) but suppressed to 0.23 m^2/s. The reduction in the smoke production rate is responsible for the condensed phase which could be attributed to the control of the fire resistance exerted on the VE/BF composites by the inclusion of NCS. (Song et al. 2014). Overall, the UL-94 test, LOI, microcalorimetry and cone calorimetry results indicated that, the NCS additive can serve as an FR for NF polymer composites by producing carbonaceous silicate char. A plausible FR mechanism of the NCS-VE/FF composite during the combustion process is shown in Scheme 2.

Char analysis The SEM images of the residual char surfaces of the VE/BF, 2%NCS-VE/BF, 4%NCS-VE/BF, and 6%NCS-VE/BF composites after the HBT are shown in Fig. 7. The VE/BF composites showed a thin and loose flakes kind of brittle scarred char produced through quick evaporation of the condensed phase. As a result, the intensity of the fire propagation increased by allowing the two factors in the fire triangle, i.e., oxygen and heat. However, the incorporation of NCS into VE/BF composites exhibited dense and continual char formation, which may exclude flammable gases and prevent the propagation of combustion. The gradual improvement in compact char formation could be observed at higher loadings of the NCS additive. In addition, the SEM-EDX analysis identified the major elements present in the char residue of the VE/BF and NCS-VE/BF composites. The VE/BF contained primarily C and O, referred to as carbonaceous char. However, the NCS-VE/BF composites displayed Si in the char along with C and O. The % of Si and O increased and the % of C decreased in the char residue in the 4 and 6 wt.% NCS-VE/BF composites which means that crystalline SiO_2 was present in the char residue.

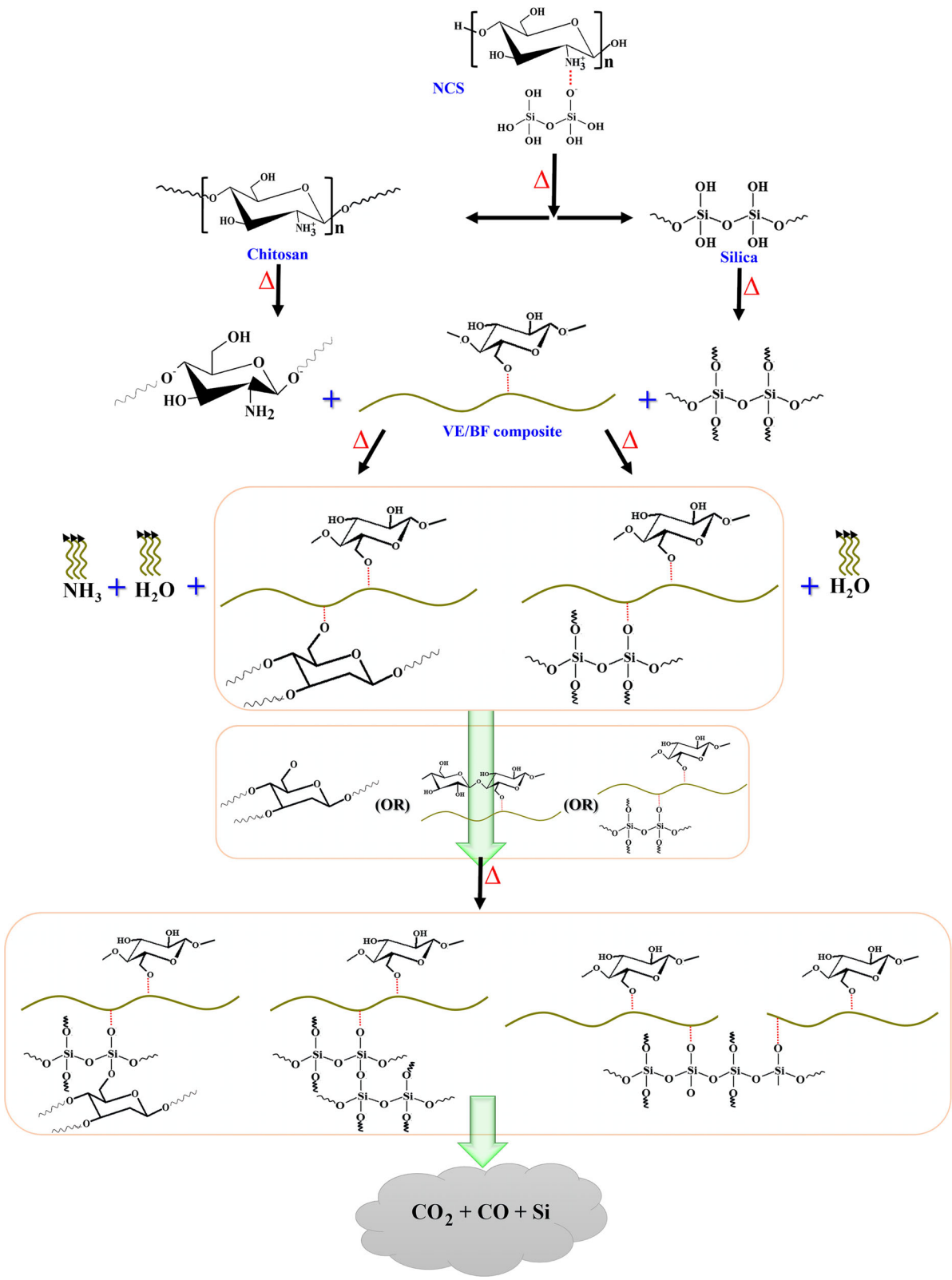
NCS
Chitosan
Silica
VE/BF composite
(OR)
(OR)
NH_3
H_2O
H_2O
$CO_2 + CO + Si$

◀**Scheme 2** Plausible FR mechanism of NCS-VE/FF composite during the combustion process

Mechanical performance

Tensile properties An evident increase in the tensile properties of the VE/BF composite was observed as a result of the NCS addition. The tensile test results are presented in Fig. 8 and Table 3, along with error bars. The tensile strength of VE/BF was increased by 29.5% after the addition of 6% NCS. The tensile strength values of the composites are in the order of 2% NCS–VE/BF (30.73 MPa) > 4% NCS–VE/BF (30.42 MPa) > VE/BF (27.95 MPa) 6% NCS–VE/BF (26.29 MPa). The addition of NCS in NF-based polymer composites generally reduces their tensile strength and interfacial bonding due to the noncompatibility of the particles with the fibers and polymers; this has been frequently reported in the literature (Fang et al. 2020; Liu et al. 2012). However, in this study, the NCS particles enhanced the interfacial bonding of the BF with VE and hence increased the tensile strength of the composites. This increase in the tensile strength supports -OH interactions between the NCS particles and VE/BF composites, as revealed in the FTIR analysis. These results also verify the fine dispersion of the NCS particles in the composites, as evident from the SEM images of the composite surfaces. The deposition of the NCS particles on the BF surfaces enhanced the interfacial bonding with the VE matrix, which resulted in a reduced number of fiber pull-outs during tensile fracture, as is evident from the SEM fractographs in Fig. 5. The decrease in the fiber pull-out spots in the NCS-filled VE/BF composites indicates enhanced interfacial bonding between the fibers and the matrix. The friction at the interfaces between the fibers and the matrix in the presence of NCS facilitates the transfer of load from the matrix to the fibers, thereby causing a dominant fiber breakout failure instead of fiber pull-outs.

The higher stiffness of the NCS particles compared to those of the BFs and VE also demonstrates its effect, resulting in the higher tensile modulus of the NCS-VE/BF composites. The results indicate that the tensile modulus of the VE/BF composite increased after the incorporation of the NCS particles. The tensile moduli of the composites are in the order of 6% NCS–VE/BF (2.36 GPa) > 4% NCS–VE/BF (1.76 GPa) > 2% NCS–VE/BF (1.68 GPa) > VE/BF (1.57 GPa). The increase in the tensile modulus is also attributed to the enhanced interfacial bonding between the fibers and the matrix in the presence of NCS particles. In the NCS-filled VE/BF composites, the load is largely transferred to the BF, which has a higher tensile modulus than that of the VE matrix, causing the tensile moduli of these composites to increase. A similar trend has been reported in the literature regarding the tensile moduli of other particulate-filled NF composite materials (Chee et al. 2021; Beigloo et al. 2020).

Flexural properties An increase in the flexural properties was observed after incorporating NCS

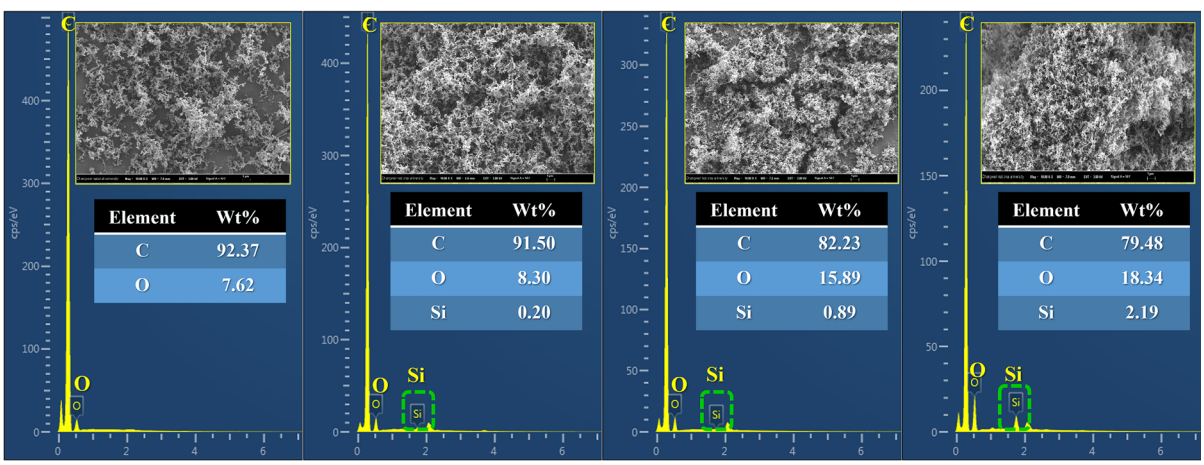

Fig. 7 Char SEM micrographs and EDX analysis results of VE/BF and 2–6% NCS-loaded VE/BF composites

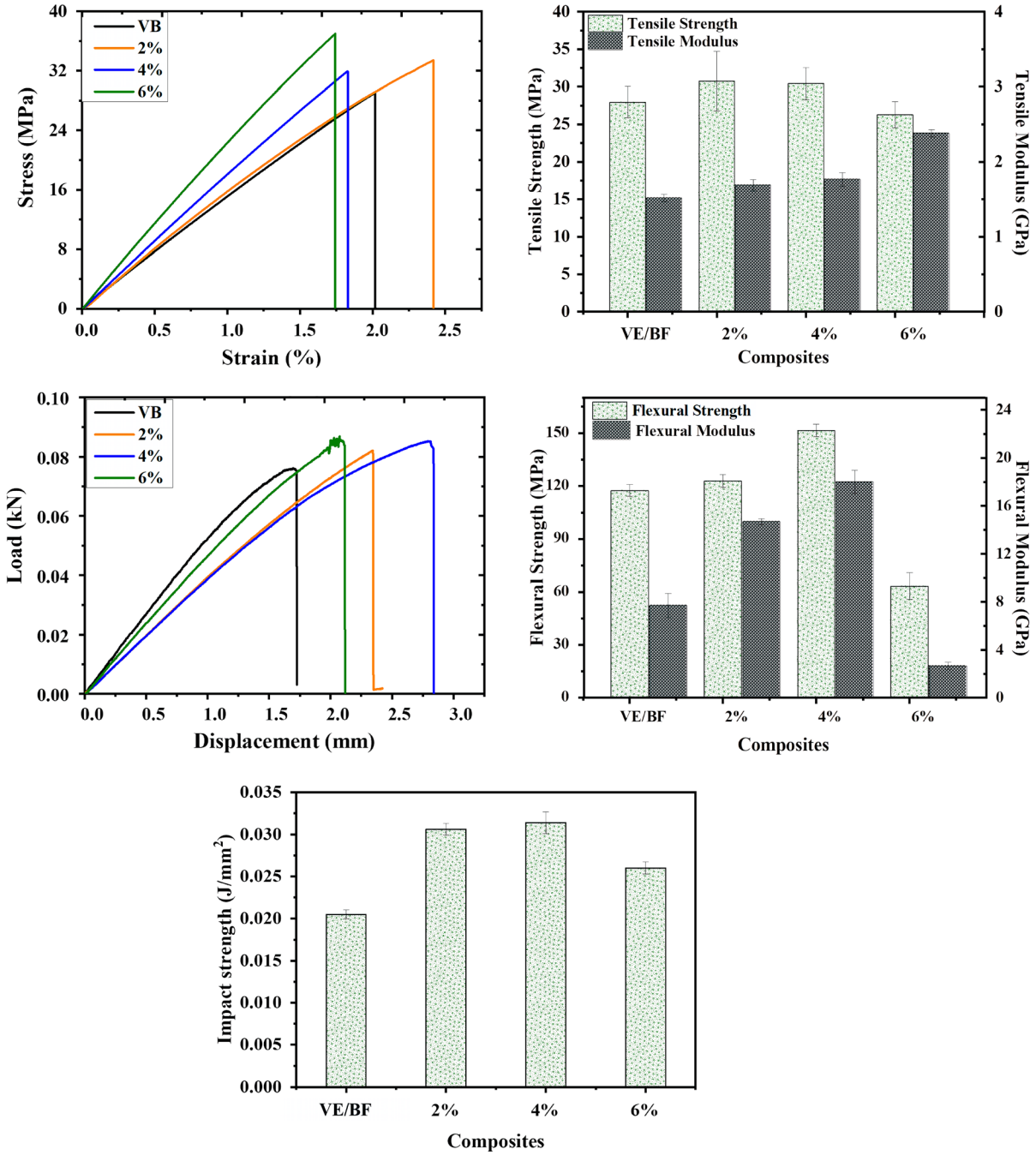

Fig. 8 Tensile strength and modulus (**a**), flexural strength and modulus (**b**) and Izod notched impact strength of VE/BF and 2–6% NCS loaded VE/BF composites

particles into the VE/BF composite. The results of the three-point bending test are summarized in Fig. 8 and Table 3. The maximum flexural strength was observed after incorporating 4% NCS particles into the VE/BF composite. The increase in the flexural strength of the 4% NCS–VE/BF composite was 15.5% that of the VE/BF composite. The flexural strengths of the composites follow the order 4% NCS–VE/BF (151.65 MPa) > 2% NCS–VE/BF (122.89 MPa) > VE/BF (117.53 MPa) > 6% NCS–

Table 3 Tensile strength and modulus (A), flexural strength and modulus (B) and Izod notched impact strength of VE/BF and 2–6% NCS-loaded VE/BF composites

	Tensile strength (MPa)	Tensile modulus (GPa)	Flexural strength (MPa)	Flexural modulus (GPa)	Impact strength (J/mm)
VE/BF	27.95	1.57	117.53	2.88	0.0205
2%NCS-VE/BF	30.73	1.68	122.89	3.08	0.0306
4%NCS-VE/BF	30.42	1.76	151.65	3.22	0.0314
6%NCS-VE/BF	26.29	2.36	63.32	3.99	0.0260

VE/BF (63.32 MPa). The increase in the flexural strength of the composites occurred for the same reason as the increase in the tensile strength. The compatibility of NCS particles, their interaction with BF, and the fine distribution of the particles in the VE resin enhanced the interfacial bonding between the resin and the reinforcement. The distribution of NCS particles in the VE/BF composite can be observed in the SEM images of composite surfaces in Fig. 4. The interaction of NCS with the VE/BF composite was explained based on the FTIR analysis results. A decrease in the flexural strength of the VE/BF composite was observed after the NCS loading exceeded 4 wt%. The 6% NCS–VE/BF composite exhibited the lowest flexural strength. The low flexural strength at a high loading of NCS particles in the VE/BF composite may be attributed to the agglomeration of the particles, causing a higher stress concentration.

The flexural modulus of the composites also increased after loading the NCS particles in the VE/BF composite. The 4 wt% NCS-incorporated VE/BF composite displayed the highest flexural modulus, which was 2.33 times that of the basic VE/BF composite. The flexural modulus of the composites followed the order 4% NCS–VE/BF (18.01 GPa) > 2% NCS–VE/BF (14.68 GPa) > VE/BF (7.7 GPa) > 6% NCS–VE/BF (2.2 GPa). The increase in the flexural modulus of the VE/BF composite after the incorporation of NCS was attributed to the compatibility and enhanced interfacial bonding. The higher flexural and tensile moduli also ensured higher thermal stability of the VE/BF composites in the presence of NCS particles.

Impact properties The ability of the VE/BF composites to absorb energy before impact failure was observed to increase after the incorporation of NCS particles. The results of the Izod impact test are summarized in Fig. 8 and Table 3. The VE/BF composite with 4 wt% NCS particles absorbed the highest amount of energy in the impact test, which was 53% of that of the VE/BF composite. The composites absorbed the impact energy in the following order: 4% NCS–VE/BF (0.0314 J/mm) > 2% NCS–VE/BF (0.0306 J/mm) > 6% NCS–VE/BF (0.026 J/mm) > VE/BF (0.0205 J/mm). The impact properties of the composites were observed to decrease after NCS loading exceeded 4 wt%. The 6% NCS–VE/BF composite absorbed a lower impact energy than the other NCS-filled VE/BF composites, which may be due to the agglomeration of particles, causing stress concentration and hence rapid failure. The rigidity of the NCS particles as compared to the VE resin also enhances the impact properties of the VE/BF composites. A similar trend regarding the enhancement in the impact properties of NF-based polymer composites caused by FR particles has been reported in the literature (Raghul et al. 2021; Bozkurt et al. 2017).

Conclusions

In this study, CS was successfully modified to a superior FR and thermally stable form (NCS) by a simple chemical method. Characterization techniques such as SEM, elemental analysis, FTIR, XRD, TGA, and microcalorimetry proved the chemical formation of NCS and its thermal and FR properties. NCS–VE/

BF composites showed satisfactory flame retardancy and thermal stability compared to VE/BF composites: a delayed burning time of approximately 40%, an enhanced LOI of approximately 33%, an HRR reduction of approximately 14%, and an enhancement in the char residue as a result of TGA were observed. Interestingly, incorporation of the NCS additive also improved the tensile, flexural, and impact properties of the VE/BF composites. Furthermore, SEM analysis demonstrated a homogeneous distribution of the additives, which was the main factor responsible for changing the properties of the composites. In brief, the above results confirmed that NCS could be used as an FR in NF composites to achieve improved mechanical strength and thermal stability.

Acknowledgments This study was supported by the Basic Science Research Program through the National Research Foundation of Korea (NRF) funded by the Ministry of Science Education (2018R1A6A1A03024509 and 2021R1A2B5B03002355).

Declarations

Conflict of interest The authors declare no conflict of interest.

Consent to participate All the authors give explicit consent to participate and submit the article.

Consent for publication The authors obtained consent for publication from the responsible authorities at the institute where the work was carried out.

Human and animal rights The authors carried out no animal or human studies.

Ethics approval All the authors agree with the content of the article.

References

Atta Ur Rehman S, Prabhakar MN, Wang H, Ji S (2018) The influence of particle size and surface treatment of filler on the properties of oyster shell powder filled polypropylene composites. Polym Compos 39:2420–2430. https://doi.org/10.1002/pc.24225

Beigloo JG, Khademi Eslam H, Hemmasi AH et al (2020) Nanographene's influence on a recycled high-density polyethylene/poplar wood flour nanocomposite. Bioresources 15:1233–1251. https://doi.org/10.15376/biores.15.1.1233-1251

Bozkurt ÖY, Özbek Ö, Abdo AR (2017) The effects of nanosilica on charpy impact behavior of glass/epoxy fiber reinforced composite laminates. Period Eng Nat Sci. https://doi.org/10.21533/pen.v5i3.119

Budnyak T, Tertykh V, Yanovska E (2014) Chitosan immobilized on silica surface for wastewater treatment. Mater Sci (medziagotyra) 20:177–182. https://doi.org/10.5755/j01.ms.20.2.4975

Chalapathi KV, Song J, Prabhakar MN (2020) Impact of surface treatments and hybrid flame retardants on flammability, and thermal performance of bamboo fabric composites. J Nat Fibers. https://doi.org/10.1080/15440478.2020.1798849

Chee SS, Jawaid M, Alothman OY, Fouad H (2021) Effects of nanoclay on mechanical and dynamic mechanical properties of bamboo/kenaf reinforced epoxy hybrid composites. Polymers 13:395. https://doi.org/10.3390/polym13030395

Costes L, Laoutid F, Brohez S, Dubois P (2017) Bio-based flame retardants: when nature meets fire protection. Mater Sci Eng R Rep 117:1–25. https://doi.org/10.1016/j.mser.2017.04.001

Elsabbagh A, Attia T, Ramzy A et al (2018) Towards selection chart of flame retardants for natural fibre reinforced polypropylene composites. Compos B Eng 141:1–8. https://doi.org/10.1016/j.compositesb.2017.12.020

Fang L, Lu X, Zeng J et al (2020) Investigation of the flame-retardant and mechanical properties of bamboo fiber-reinforced polypropylene composites with melamine pyrophosphate and aluminum hypophosphite addition. Materials (basel) 13:479. https://doi.org/10.3390/ma13020479

Hamdani S, Longuet C, Perrin D et al (2009) Flame retardancy of silicone-based materials. Polym Degrad Stab 94:465–495. https://doi.org/10.1016/j.polymdegradstab.2008.11.019

Hassan H, Salama A, El-Ziaty AK, El-Sakhawy M (2019) New chitosan/silica/zinc oxide nanocomposite as adsorbent for dye removal. Int J Biol Macromol 131:520–526. https://doi.org/10.1016/j.ijbiomac.2019.03.087

Hung X, Cen D, Wei R, Hualin F, Bao Z (2019) Synthesis of porous Si/C composite nanosheets from vermuculite with a hierarchical strcture as a high performance anode for lithium-ion battery. ACS Appl Mater Interfaces 11:26854–26862. https://doi.org/10.1021/acsami.9b06976

Jeencham R, Suppakarn N, Jarukumjorn K (2014) Effect of flame retardants on flame retardant, mechanical, and thermal properties of sisal fiber/polypropylene composites. Compos B Eng 56:249–253. https://doi.org/10.1016/j.compositesb.2013.08.012

Khalili P, Tshai KY, Kong I (2017) Natural fiber reinforced expandable graphite filled composites: evaluation of the flame retardancy, thermal and mechanical performances. Compos Part A Appl Sci Manuf 100:194–205. https://doi.org/10.1016/j.compositesa.2017.05.015

Kim NK, Bruna FG, Das Oisik et al (2020) Fire-retardancy and mechanical performance of protein-based natural fibre-biopolymer composites. Compos C. https://doi.org/10.1016/j.jcomc.2020.100011

Kumar S, Koh J (2012) Physiochemical, optical and biological activity of chitosan-chromone derivative for biomedical applications. Int J Mol Sci 13:6102–6116. https://doi.org/10.3390/ijms13056102

Kuranchie C, Yaya A, Bensah YD (2021) The effect of natural fibre reinforcement on polyurethane composite foams—a review. Sci Afr 11:e00722. https://doi.org/10.1016/j.sciaf.2021.e00722

Lau K-T, Hung P-Y, Zhu M-H, Hui D (2018) Properties of natural fibre composites for structural engineering applications. Compos B Eng 136:222–233. https://doi.org/10.1016/j.compositesb.2017.10.038

Li P, Liu C, Xu Y-J et al (2020) Novel and eco-friendly flame-retardant cotton fabrics with lignosulfonate and chitosan through LbL: Flame retardancy, smoke suppression and flame-retardant mechanism. Polym Degrad Stab. https://doi.org/10.1016/j.polymdegradstab.2020.109302

Liu SJ, Han YM, Zhu RX et al (2012) Effect of flame retardant on combustion and mechanical properties of bamboo-fiber based composites. Adv Mater Res 488–489:597–601

Lustriane C, Dwivany FM, Suendo V, Reza M (2018) Effect of chitosan and chitosan-nanoparticles on post harvest quality of banana fruits. J Plant Biotechnol 45:36–44. https://doi.org/10.5010/JPB.2018.45.1.036

Porsche Newsroom (2019) New Porsche 718 Cayman GT4 Clubsport featuring natural-fibre body panels. https://newsroom.porsche.com/en/products/porsche-world-premiere-new-718-cayman-gt4-clubsport-16733.html

Pan M, Mei Changtong DuJ, Guochen Li (2014) Synergistic effect of Nano silicon dioxide and ammonium polyphosphate on flame retardancy of wood fiber–polyethylene composites. Compos Part A Appl Sci Manuf 66:128–134. https://doi.org/10.1016/j.compositesa.2014.07.016

Prabhakar MN, Song JI (2018) Fabrication and characterisation of starch/chitosan/flax fabric green flame-retardant composites. Int J Biol Macromol 119:1335–1343. https://doi.org/10.1016/j.ijbiomac.2018.07.006

Prabhakar MN, Song J (2020) Influence of chitosan-centered additives on flammable properties of vinyl ester matrix composites. Cellulose 27:8087–8103. https://doi.org/10.1007/s10570-020-03313-4

Prabhakar MN, Raghavendra GM, Vijaykumar BVD et al (2019) Synthesis of a novel compound based on chitosan and ammonium polyphosphate for flame retardancy applications. Cellulose 26:8801–8812. https://doi.org/10.1007/s10570-019-02671-y

Raghul KS, Logesh M, Kisshore RK et al (2021) Mechanical behaviour of sisal palm glass fiber reinforced composite with addition of nano silica. Mater Today Proc 37:1427–1431. https://doi.org/10.1016/j.matpr.2020.07.063

Sain M, Park SH, Suhara F, Law S (2004) Flame retardant and mechanical properties of natural fibre–PP composites containing magnesium hydroxide. Polym Degrad Stab 83:363–367. https://doi.org/10.1016/S0141-3910(03)00280-5

Satheesh Kumar S (2020) Dataset on mechanical properties of natural fiber reinforced polyester composites for engineering applications. Data Brief 28:105054. https://doi.org/10.1016/j.dib.2019.105054

Sefadi JS, Luyt AS (2012) Morphology and properties of EVA/empty fruit bunch composites. J Thermoplast Compos Mater 25:895–914. https://doi.org/10.1177/0892705711421806

Shao ZB, Deng C, Tan Y, Yu L, Chen MJ, Chen L, Wang YZ (2014) Ammonium polyphosphate chemically modified with ethanolamine as an efficient intumescent flame retardant for polypropylene. J Mater Chem A 2:13955–13965. https://doi.org/10.1039/c4ta02778g

Shao N, Qu Y, Hu Y, Tian Z, Gao Y, Zhu X (2021) Effect of starch-based flame retardant on the thermal degradation and combustion properties of reconstituted tobacco sheet. Cellulose 28:741–755

Shen Y, Zhao P, Qinfu S (2014) Porous silica and carbon derived materials from rice husk pyrolysis char. Micropor Mesopor Mater 188:46–76. https://doi.org/10.1016/j.micromeso.2014.01.005

Shukor F, Hassan A, Saiful Islam Md et al (2014) Effect of ammonium polyphosphate on flame retardancy, thermal stability and mechanical properties of alkali treated kenaf fiber filled PLA biocomposites. Mater Des 1980–2015(54):425–429. https://doi.org/10.1016/j.matdes.2013.07.095

Song S, Ma J, Cao K, Chang G, Huang Y, Yang J (2014) Synthesis of a novel dicyclic silicon-/phosphorus hybrid and its performance on flame retardancy of epoxy resin. Polym Degrad Stab 99:43–52. https://doi.org/10.1016/j.polymdegradstab.2013.12.013

Wang J, Shanye Y, Ma R (2020) Synthesis and characterization of sodium laurylsulfonate modified silicon dioxide for the efficient removal of europium. J Mol Liq. https://doi.org/10.1016/j.molliq.2020.113846

Yeh J-T, Chen C-L, Huang K-S (2007) Synthesis and properties of chitosan/SiO2 hybrid materials. Mater Letter 61:1292–1295. https://doi.org/10.1016/j.matlet.2006.07.016

Yingji Wu, Cai L, Changtong M et al (2020) Development and evaluation of zinc oxide-blended kenaf fiber biocomposite for automotive applications. Mater Today Commun. https://doi.org/10.1016/j.mtcomm.2020.101008